Disruption of myelin structure and oligodendrocyte maturation in a pigtail macaque model of congenital Zika infection

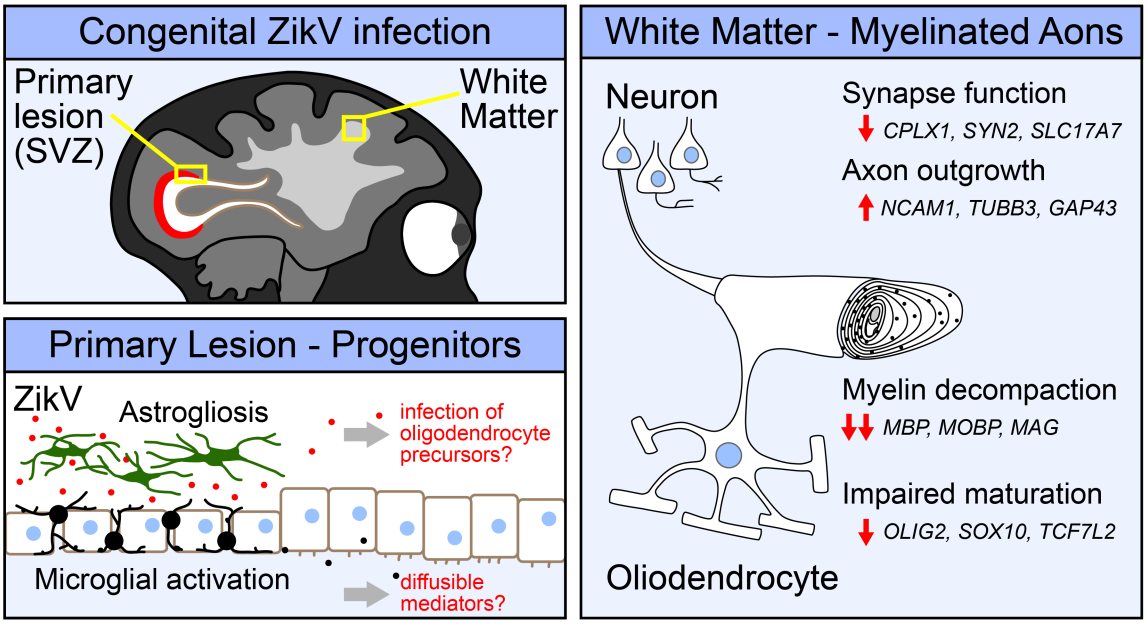

Graphical abstract (also **Fig. S8** – see supplemental information for figure legend)

Jennifer Tisoncik-Go[1,*], Caleb Stokes[1,2,*], Leanne S. Whitmore[1], Daniel J. Newhouse[1], Kathleen Voss[1], Andrew Gustin[1], Cheng-Jung Sung[1], Elise Smith[1], Jennifer Stencel-Baerenwald[1], Edward Parker[3], Jessica M. Snyder[4], Dennis W. Shaw[5], Lakshmi Rajagopal[2,6,7,], Raj P. Kapur[8,9], Kristina Adams Waldorf[7,10,11], and Michael Gale Jr.[1,7,10]

Affiliations:

[1]Center for Innate Immunity and Immune Disease, Department of Immunology, University of Washington, Seattle, Washington, USA

[2]Department of Pediatrics, University of Washington, Seattle, Washington, USA

[3]Department of Ophthalmology, NEI Core for Vision Research, University of Washington, Seattle, Washington, USA

[4]Department of Comparative Medicine, University of Washington, Seattle, Washington, USA

[5]Department of Radiology, University of Washington, Seattle Washington, USA

[6]Center for Global Infectious Disease Research, Seattle Children's Research Institute, Seattle, Washington, USA

[7]Department of Global Health, University of Washington, Seattle, Washington, USA

[8]Department of Pathology, University of Washington, Seattle, Washington, USA

[9]Department of Pathology, Seattle Children's Hospital, Seattle, Washington, USA

[10]Department of Obstetrics & Gynecology, University of Washington, Seattle, Washington, USA

[11]Sahlgrenska Academy, Gothenburg University, Gothenburg, Sweden

[*]These authors contributed equally to this work

Contact: Correspondence should be addressed to MG (mgale@uw.edu) and KAW (adamsk@uw.edu)

Additional Footnotes:

Abstract

Zika virus (ZikV) infection during pregnancy can cause congenital Zika syndrome (CZS) and neurodevelopmental delay in non-microcephalic infants, of which the pathogenesis remains poorly understood. We utilized an established pigtail macaque maternal-to-fetal ZikV infection/exposure model to study fetal brain pathophysiology of CZS manifesting from ZikV exposure *in utero.* We found prenatal ZikV exposure led to profound disruption of fetal myelin, with extensive downregulation in gene expression for key components of oligodendrocyte maturation and myelin production. Immunohistochemical analyses revealed marked decreases in myelin basic protein intensity and myelinated fiber density in ZikV-exposed animals. At the ultrastructural level, the myelin sheath in ZikV-exposed animals showed multi-focal decompaction consistent with perturbation or remodeling of previously formed myelin, occurring concomitant with dysregulation of oligodendrocyte gene expression and maturation. These findings define fetal neuropathological profiles of ZikV-linked brain injury underlying CZS resulting from ZikV exposure *in utero*. Because myelin is critical for cortical development, ZikV-related perturbations in oligodendrocyte function may have long-term consequences on childhood neurodevelopment, even in the absence of overt microcephaly.

Main

Maternal infection during pregnancy can have severe consequences on fetal development and survival. Zika virus (ZikV) is an emerging flavivirus that can be vertically transmitted to the fetus from an infected pregnant mother, leading to congenital Zika syndrome (CZS), which encompasses a range of fetal malformations including hearing loss, ocular manifestations, intrauterine growth restriction, and microcephaly[1-4], as well as miscarriage[5-7]. CZS persists post-partum and imposes major complications to childhood development, now manifested across ZikV-endemic regions[8,9]. While the mechanism of microcephaly in CZS is thought to be related to ZikV infection and death of neural progenitor cells leading to decreased neurogenesis[10-12], the pathogenesis of neurodevelopmental delay in CZS displaying normal brain development, termed “normocephalic”, is poorly understood. Important questions remain in understanding the impact of ZikV infection on prenatal development, and perhaps chief among these is the question of how ZikV causes neurologic injury in CZS, including among normocephalic outcomes.

Neuronal remodeling and myelination are major processes that account for central nervous system (CNS) growth and maturation[13]. Myelin, an extension of the lipid membrane of oligodendrocytes, wraps around axons and plays a critical role in neuronal function by insulating and facilitating efficient transmission of electrical signals along the axon[14]. In humans, myelination initiates as early as the fifth fetal month within the caudal brain stem and progresses rostrally to the forebrain, with rapid additional development within the first two years of postnatal life[15-17]. Formation of myelin by oligodendrocytes is necessary for the development of complex neurologic circuits that underlie movement, sensory processing, cognition, and memory[18-22]. However, in fetal development the myelinated axons in the deep cortex are uniquely susceptible to injury by hypoxia and inflammation[23].

Nonhuman primate (NHP) models of ZikV infection in pregnancy recapitulate aspects of vertical transmission, fetal neuropathology, fetal demise, and miscarriage observed in humans[24-27]. We have established an NHP model of congenital ZikV infection in pregnancy wherein maternal to

fetal virus transmission can result in fetal neuropathology with microcephaly[28] or without microcephaly[29], reflecting human CZS. Here, we employ a systems biology approach to characterize CZS and define fetal demyelinating disease following maternal-to-fetal ZikV transmission in mid-to-late gestation in the context of otherwise normocephalic fetal development. Spatial transcriptomic, bulk mRNA sequencing (RNAseq), magnetic resonance imaging (MRI), histopathologic and virologic analyses of fetal brain tissue reveal that ZikV-exposed fetuses have extensive changes in white matter histology, gene expression, and specific protein levels occurring independent of microcephaly and are sustained after ZikV RNA is cleared from the tissue. These alterations include genes that span all maturational stages of oligodendrocyte development and reveal specific tissue disorganization with altered oligodendrocyte morphology within brain lesions following fetal exposure to ZikV. The structure of myelin in ZikV-exposed fetuses is perturbed and, in the most severely affected animals, there is evidence of oligodendrocyte injury and axonal dysfunction. These findings indicate that oligodendrocyte alteration leading to dysregulation of myelination and myelin wrap maintenance are features of CZS. Since altered myelination in CZS can occur in the absence of microcephaly, our findings implicate oligodendrocyte dysregulation and myelin disruption as an underlying feature of CZS that could impact pre- and post-natal neurologic development in children with CZS.

Results

In an established nonhuman primate model of transplacental Zika virus transmission, we investigated neuropathological changes in fetal white matter after maternal ZikV infection during pregnancy using spatial and bulk tissue transcriptomics, immunohistochemistry (IHC), electron microscopy (EM) and magnetic resonance imaging (MRI) analyses. We conducted a cohort study of 6 maternal ZikV challenge animals who received ZikV subcutaneously at times ranging from 60-121 gestation days (GD), and 6 control animals who received saline (at 59-138 GD) instead of virus

challenge (**Fig. S1a and Table S1**). Animals ZikV1 and ZikV2 were challenged with ZikV/FSS13025/Cambodia[28], while animals ZikV 3-6 were challenged with ZikV/Brazil/Fortaleza/2015[29] (**Table S1**). Each fetus was delivered by Cesarean section at gestational ages ranging from 141-159 days, corresponding to late third trimester (**Table S2**). Within the ZikV challenge cohort, transient viremia was demonstrated across 6/7 ZikV-challenged dams at 2 days post-infection (DPI), with ZikV RNA detected in fetal brain at necropsy of 3/6 ZIKV cohort animals (**Fig. S1d**)[29].

To define fetal brain transcriptome changes following maternal infection with ZikV, we used spatial transcriptional profiling to identify gene expression patterns from discrete regions of interest (ROIs) in developing parietal cortex. We chose ROIs representing functionally distinct compartments as follows: grey matter (DGM, containing cortical Layer V pyramidal neuron cell bodies), superficial white matter (SWM, containing proximal axons in cortical Layer VI), and deep white matter (DWM, containing myelinated axons of projecting neurons deep to the cortex) (**Fig.1a**). ROI-specific gene expression patterns matched those predicted by the predominant cell types in each region (**Fig. 1b**). With regional signatures identified in healthy controls, we next assessed the impact of ZikV exposure on gene expression (**Fig. 1c**). Our analysis indicated that the largest magnitude of ZikV-related transcriptional changes occurred in the deep white matter (**Fig. 1d-e, Fig. S2a-b, Tables S3 and S4**). The DWM of ZikV-exposed animals compared to control had markedly reduced expression (downregulation) of oligodendrocyte genes fundamental to the formation and maintenance of myelin sheaths in the central nervous system, including *MBP*, *MOBP*, *PLP1*, and *CNP* (**Fig. 1d**). In contrast, the gray matter of ZikV-exposed fetal brains showed increased expression (upregulation) of genes underlying axon growth (*NCAM1, TUBB, GAP43*), and down-regulation of genes related presynaptic function (*CLPLX1, SLC17A7, SYN2*; **Fig. 1e**) compared to control.

An over representation analysis of significantly differentially expressed genes displayed using gene network analysis across DGM and DWM fetal brain regions demonstrated downregulation of oligodendrocyte differentiation and functional genes in the DWM of ZikV exposed

fetuses; DGM changes included upregulation of neuron projection guidance, cell migration, and neuron development genes in DGM (**Fig. 1f** and **Table S5**). Upstream regulator analysis of DE genes indicated decreased activity of the transcription factor *TCF7L2,* which controls oligodendrocyte development and myelin-related gene expression[30,31]; importantly, this decrease was predicated in all three brain regions for ZikV exposed fetuses (**Fig. S2c**). This finding agreed with our identification of decreased gene expression across all maturational stages of the oligodendrocyte lineage within ZikV-exposed fetal DWM, including *SOX10 and OLIG2*[32] (**Fig. S2d).** TCF7L2 expression was downregulated in DWM although not significant by FDR test (FDR=0.19; p=0.03 by t-test). In addition, DGM (and, to a lesser extent, DWM) had downregulated genes related to synaptic signaling (e.g., *SYN2*, *SLC17A7*, and *CPLX1*). Upstream regulator analysis also predicted decreased activity of the transcription factor *SOX2* in SWM and DWM of ZikV-exposed fetuses, consistent with our previous report of reduced Sox2+ cells in neurogenic populations in the subventricular zone (SVZ) of ZikV-exposed fetuses[29].

This spatial transcriptomic analysis resolved ZikV-related gene expression changes within specific regions of parietal cortex. To examine changes of cell populations in the parietal cortex, we performed bulk RNA sequencing (RNAseq) of superficial fetal cortical samples spanning the anterior-posterior axis and used CIBERSORT[33] to deconvolve gene expression profiles to estimate the relative abundances of cell types in the tissue. The bulk RNAseq analysis demonstrated widespread transcriptional changes related to axon guidance and myelination across the fetal brain (**Fig. S3a-c**)[30-32]. Cellular deconvolution analysis indicated the proportions of cell types in fetal cortex of ZikV-exposed animals were largely unchanged relative to controls (**Fig. S3d**). In animals with ZikV RNA detectable by PCR in fetal brain, the spatial distribution spanned the parietal and occipital cortex (**Fig. S1e**, **Fig. S3e**).

To further characterize myelin and oligodendrocytes, we analyzed white matter cellular composition by performing immunohistochemistry on parietal and occipital cortex. The expression of myelin basic protein (MBP), a key structural component of myelin, was significantly diminished in

brains of ZikV-exposed fetuses compared to controls (**Fig 2**). Qualitatively, this observation corresponded to both a reduction in the MBP staining intensity and number of MBP+ fibers in most cases (**Fig. S4a**). Luxol fast blue staining for compact myelin corroborated these findings, with decreased staining of the white matter of ZikV-exposed animals (**Fig. S4b**). There were no differences between control and ZikV-exposed fetal brain in the density of cells staining for Olig2 (**Fig. 2i**), which labels both oligodendrocyte precursors and myelinating oligodendrocytes[34,35]. There also were no significant differences in abundance of astrocytic marker, glial fibrillary acidic protein (GFAP), or microglial marker, allograft inflammatory factor 1 (AIF-1/Iba1), in parietal cortex with respect to ZikV exposure (**Fig. S4e-f**), or the density of NeuN-positive neurons in any layers of cortex, either in occipital or parietal cortex (**Fig. S6**). However, we found a local increase in the GFAP intensity and microglia density in the ependymal lining of the posterior lateral ventricle of ZikV exposed animals, corresponding to a T2-bright primary lesion on MRI (**Fig. S5**). We also noted a transition zone between ciliated ependymal cells and smooth columnar epithelium, with underlying disruption in the cellular architecture (**Fig. S5d**). This observation is consistent with previous descriptions of increased GFAP-immunoreactive gliosis and microglial activation in the periventricular region within the central nervous system of a pregnant rhesus macaque ZikV infection model[26,28,29].

To assess the spatial and temporal extent of the pathophysiological changes in ZikV exposed animals, we reviewed serial magnetic resonance imaging. In addition to a previously described T2-bright posterior periventricular ("primary") lesion in ZikV-exposed animals[29], we noted T2-weighted signal abnormalities in the subcortical white matter that were absent in age-matched controls (compared at average GD123) and appeared to be persistent across multiple imaging time points (**Fig. 3a-c,** see **Fig. S1**). These findings were most pronounced in parietal and occipital regions corresponding to the primary sensory and visual areas of cortex. As T2-weighted MRI signal changes may represent abnormal myelin structure, delayed myelination, or inflammation[36], we performed histological and electron microscopic (EM) analysis of the primary lesion and the parietal cortex.

Although the white matter tissue appeared mildly vacuolated in ZikV-exposed animals compared to controls, there was no evidence of inflammatory infiltrate for either group based on hematoxylin and eosin staining (**Fig. 3d**). In the DGM overlying the site of the primary periventricular lesion, EM revealed severe disruption to the brain parenchyma that was not observed in the control, while in parietal grey matter there were less severe changes to ultrastructural architecture (**Fig. 3e**).

We further used EM to analyze the ultrastructural characteristics of axons in the white matter of parietal cortex in control and ZikV-exposed fetal brain (**Fig. 4**). In both groups, most large-diameter axons had a compact myelin sheath, with no consistent difference in axon diameter (**Fig. S7a-d**). However, the myelin in ZikV-exposed animals had numerous focal areas in which the laminar structure was disrupted, with outward bowing of the sheath and widened interlamellar spaces filled with electron-dense material (**Fig. 4b**). We refer to this finding as "myelin decompaction," as it structurally resembles a phenotype that has been described in animal models of axonal injury and in knockdown of myelin structural proteins such as MBP[37-40]. In many areas of decompacted myelin, we observed swelling of the inner lamella of the myelin sheath. We did not find evidence of myelin phagocytosis or increased density of phagocytes or other immune cells within the white matter (**Fig. S4d**). Intact regions of myelin had apparently normal ultrastructural properties, including number of wraps and wrap thickness (**Fig. 4c-d, Fig. S7e-f**). However, there was a significantly higher proportion of axons with myelin decompaction in ZikV-exposed animals as compared to controls (**Fig. 4e**). We measured the myelin g-ratio, which describes the fraction of the axon diameter composed of myelin, and may be increased in demyelinating conditions[41] or decreased in hypomyelinating conditions[19]. There were no consistent differences in the g-ratio or the slope of the regression line relating g-ratio to axon diameter across control and ZikV-exposed animals. However, in the most severely affected ZikV exposed animal (ZIKA3), we found a reduced g-ratio (**Fig. 3f-g, Fig. S7c**). Moreover, we found swelling of axonal mitochondria in ZIKA3 that is suggestive of axonal stress or injury (**Fig. S7g-h**). Overall, there were no differences in fetal disease phenotype across

ZikV animals following exposure to either ZikV strain used in our studies, showing that CSZ is not ZikV strain specific.

Together, these data demonstrate oligodendrocyte and myelin perturbation in ZikV-exposed prenatal macaque brain spanning scale from altered gene expression to changes in cellular structure and function, revealing links between myelin disease and neuronal dysfunction in CZS that may have profound consequences on childhood neurodevelopment after fetal exposure to ZikV, even in normocephalic infants.

Discussion

Neurotropic ZikV virus emerged to global importance as an etiologic agent of microcephaly and is now recognized to cause CZS, characterized by extensive motor and cognitive impairment in developing neonates[42,43]. Neurodevelopmental delay has become apparent for ZikV-exposed normocephalic infants born without microcephaly or other overt congenital anomalies[44-47]. Here, we challenged pregnant pigtail macaques in mid-gestation with Asian or American lineage ZikV, revealing similar normocephalic CZS phenotype across the fetal brain of all ZikV animals. This NHP model reveals several key points i) CZS is not ZikV strain-specific but may manifest from different viral strains following fetal exposure from maternal ZikV infection, and ii) CZS mirrors injury patterns seen in humans, offering a window into the pathophysiological mechanisms underlying CZS[26,28,29,48]. We found widespread and severe disruption of CNS myelin in fetuses (5 female/1 male) that were normocephalic and had no overt neuroanatomic abnormalities at birth. Our systems biology transcriptomic analysis involved multi-scale systematic characterization of the brain from the ZikV cohort animals, revealing altered gene expression in oligodendrocyte and neuronal development, reduction of myelin proteins, and myelin decompaction. These observations indicate that ZikV exposure can induce a demyelinating disease during prenatal development that is a feature contributing to CZS.

Due to the widespread white matter injury pattern observed in fetal brain, we propose that maternal-to-fetal transmission and infection with ZikV disrupts fetal myelin through a direct or indirect virus-imposed blockade on fetal oligodendrocyte function and maturation (**Fig. S8**). Neural progenitor cells (NPCs) are a primary cellular target of ZikV in the fetal brain, and NPC infection by ZikV disrupts cortical neuron migration[49]. In a fetal baboon model of congenital Zika infection, Gurung and colleagues found a decrease in oligodendrocyte precursor cells (OPCs) in the cerebellum[50]. Moreover, in a mouse model of ZikV infection, ZikV infects glial progenitor cells, perturbing OPC proliferation and differentiation[51-53]. In support of this mechanism, our spatial transcriptional profiling data revealed a decrease in expression of OPC-specific transcription factors OLIG2 and SOX10 in the ZikV fetal brain cohort (see **Fig. S8**). This observation also validates our previous work demonstrating a decrease in Sox2 from the subventricular zone within the NPC niche[29]. Here, fetal exposure to ZikV did not result in changes in the density of Olig2+ cells in white matter. In many conditions of neurologic injury, Olig2+ OPC populations expand and differentiate to oligodendrocytes, and this process is thought to facilitate repair and re-myelination of injured axons[54-56]. In contrast, we observed downregulation of genes spanning the oligodendrocyte lineage, suggesting a broader mechanism of oligodendrocyte dysregulation impairing cell maturation as well as myelin production.

A range of mechanisms have been identified underlying demyelinating diseases, including direct insult on developing oligodendrocytes, loss of trophic support from axonal degeneration, and immune-mediated attack. Fetal white matter is uniquely susceptible to injury. Hypoxia or infection *in utero* can cause periventricular leukomalacia (PVL), in which necrotic death of premyelinating oligodendrocytes is accompanied by astrogliosis and microglial activation[57,58]. Although we identified local disruption of tissue architecture and gliosis at the site of the posterior periventricular ZikV fetal brain lesion, we found extensive changes to myelin at distal sites throughout the brain, without necrosis or microglial activation typically observed in focal PVL. In adults, ZikV infection has been associated with autoimmune attack on myelin, including Guillain-Barré syndrome and acute myelitis,

wherein ZikV was cultured from a patient with meningoencephalitis[59-62]. Moreover, a fatal case of encephalitis in a non-pregnant woman infected with ZikV was linked with autoantibodies against myelin oligodendrocyte glycoprotein (MOG)[63]. An important distinction here is that in our study there was no histopathologic evidence of inflammatory infiltrate and minimal induction of proinflammatory pathways from the transcriptomic data in the fetal brain of the ZikV cohort animals, indicating the demyelinating phenotype is not the result of a chronic T cell-mediated autoimmune inflammatory response against myelin proteins or phagocytic attack of oligodendrocytes. It remains possible, however, that diffusible signals from the inflammatory response at the primary lesion in the brain or from other fetal tissues led to widespread perturbations in oligodendrocyte lineage maturation signaling—a mechanism that has been proposed to explain diffuse white matter injury in PVL[64,65].

Several animal models of CNS injury have described a similar phenotype of myelin decompaction, most notably the optic nerve crush model that is used to study demyelination and axon regeneration[37,66,67]. While the precise mechanisms of myelin decompaction are areas of active investigation, acute knockdown of myelin structural components (e.g., MBP) can lead to a similar phenotype[40], suggesting that active signaling and protein synthesis are necessary to maintain compact myelin. Additionally, oligodendrocyte maturation and myelin synthesis are closely coupled to neuronal maturation and function in a bidirectional manner[68]. Therefore, we propose that the disruption of myelin may be related to a loss of trophic support from local neurons or even astrocytes[39] (**Fig. S8**). Indeed, our spatial transcriptional data from deep grey matter shows a decrease in expression of genes for synaptic function and an increase in genes related to axon outgrowth in ZikV cohort animals. We note that in a mouse model of flavivirus encephalitis recovery, ZikV infection leads to loss of synapses[69]. The gene networks we observed in DGM may therefore represent remodeling of neuronal circuits in response to loss of synapses. This type of developmental neuroplasticity is a well-described phenomenon in which neurons that experience a loss of functional connectivity undergo axonal outgrowth in order to find new synaptic partners[70,71], and could be a widespread response to focal ZikV infection in the fetal brain affected by CZS[69].

The risk of recurrent ZikV outbreaks in endemic regions due to waning population immunity or new epidemics due to ZikV introduction into naïve populations remains a lingering threat, with a major impact resulting from maternal infections during pregnancy[72,73]. Emerging infectious diseases have the greatest impact in immunologically naïve populations and at risk individuals, such as pregnant women and their unborn, as further demonstrated by the recent SARS-CoV2 pandemic[74,75]. Understanding how ZikV impacts cellular processes during prenatal development is necessary to develop therapeutic strategies for preventing CZS and mitigating ZikV infection. These findings reinforce the serious nature of ZikV infection, and virus infection during pregnancy in general, and the need for effective vaccines or drugs to prevent congenital infections. Our study adds to these findings by providing additional insight into the pathophysiology of CZS following ZikV fetal exposure, including ultrastructural features of myelin decompaction, oligodendrocyte dysregulation, and changes to neuronal function and signaling, that underlie CZS.

3097 words.

Methods

Virus. Working stocks of ZIKV/Brazil/Fortaleza/2015 (GenBank no. KX811222) and ZIKV/FSS13025/Cambodia (GenBank no. MH368551) were obtained by plaque-purifying the viruses and amplifying once in C6/36 *Aedes albopictus* cells. Virus was adsorbed to cells in DMEM supplemented with 1% FBS at 37°C. After 2-hours incubation, the inoculum was removed and virus propagated in complete media supplemented with 5% FBS, 2 mM L-Glutamine, 1 mM Sodium Pyruvate, 100 U/mL of Penicillin, 100 µg/mL of Streptomycin, 20 mM HEPES, and 1X MEM Non-essential Amino Acid Solution for 6 days, with media changed at 3 days post-inoculation. Supernatants at 6 days were then collected and centrifuged at 2,000 RPM at 4°C for 10 min, and frozen in aliquots at -80°C. Virus stocks were tittered on Vero cells.

Study Design. The nonhuman primate experiments were carried out in strict accordance with the recommendations in the Guide for the Care and Use of Laboratory Animals of the National Research Council and the Weatherall report, “The use of non-human primates in research”. The Institutional Animal Care and Use Committee of the University of Washington approved the study (Permit Number: 4165-02). There were a total of twelve, healthy pregnant pigtail macaques (*Macaca nemestrina; Mn*) (**Fig. S1**). ZikV inoculation was administered to resemble the bite of a feeding mosquito. ZIKA1 and ZIKA2**,** received subcutaneous (s.c.) inoculations of ZIKV/FSS13025/Cambodia at five separate locations on the forearms, each with 10^7 plaque-forming units (PFU) in their mid-late second trimester of pregnancy, while ZIKA3-6 received similar s.c. inoculations of ZIKV/Fortaleza/Brazil/2015 at five separate locations on the forearms, each with 10^7 PFU. Six pregnant control animals, CTL1-6, received s.c. inoculations of media alone at five separate locations on the forearms. Cesarean section was performed at least 10 days before the natural due date (~172 days) to enable fetal and dam necropsy (**Table S1**). Fetal brains were weighed at birth and sectioned (**Table S2**).

Digital Spatial Profiling. Fixed, paraffin-embedded NHP fetal brain sections representing parietal cortex were prepared according to the GeoMx-DSP Slide Preparation User Manual (NanoString, Inc, MAN-10115-04). Unstained 5µm-thick tissue sections mounted on Colorfrost microscope slides (Fisher Scientific) were used for GeoMx Digital Spatial Profiling (DSP; NanoString, Inc.) assay. RBFOX3 (NeuN), GFAP, and Olig2 cellular markers were used to characterize the tissue morphology and select regions of interest (ROIs) for profiling (**Table S10**). *In situ* hybridizations were performed with the GeoMx Human Whole Transcriptome Atlas Panel (WTA, 18,676 total targets) according to the manufacturer's instructions. One slide at a time, probes were added to each slide in a hybridization chamber, covered with a coverslip, and incubated at 37°C overnight. Following incubation, the slides were washed to remove unbound probe and blocked in 200 µl Buffer W and incubated in a humidity chamber. Rabbit polyclonal anti-Olig2 antibody (Millipore Cat # AB9610) was incubated first at 1:100 in Buffer W, followed by Goat anti-rabbit AF647 (ThermoFisher Catalog #A27040) for visualization. The remaining morphology markers were collectively diluted in Buffer W at the following concentrations: 1:50 RBFOX3 (NeuN) (Abcam EPR12763 Catalog #ab190195), 1:400 GFAP (Novus GA5, Catalog # NBP-33184DL594, and STYO 83 for nuclei visualization for a total volume of 200 µl per slide. Each slide was scanned with a 20X objective and default scan parameters. For each tissue section, geometric 500 µm diameter circle ROIs were placed in the following regions based on assessment by a Pathologist 1) subcortex (Subcortical WM; n=3/section), 2) WM tracts (Deep WM; n=3/section), and 3) cortical layers IV-VI (GM; n=3/section). After ROI placement, the GeoMx DSP instrument photocleaves the UV cleavable barcoded linker of the bound RNA probes from each ROI and collects the individual segmented areas into separate wells in the DSP collection plate.

Library preparation and generation of expression matrices. Total target counts per DSP collection plate for sequencing were calculated from the total samples areas (μm^2). For sequencing

of whole transcriptome analysis (WTA) libraries, the target sequencing depth was 100 counts/μm^2. Sequencing libraries were generated by polymerase chain reaction (PCR) from the photo-released indexing oligos and ROI-specific Illumina adapter sequences and unique i5 and i7 sample indices were added. Each PCR reaction used 4µl of indexing oligos, 4µl of indexing primer mix and 2µl of Nanostring 5X PCR Master Mix. Thermocycling conditions were 37°C for 30 min, 50°C for 10 min, 95°C for 3 min; 18 cycles of 95°C for 15 sec, 65°C for 1 min, 68°C for 30 sec; and 68°C 5 min. PCR reactions were pooled and purified twice using AMPure XP beads (Beckman Coulter, A63881) according to manufacturer's protocol. Pooled libraries were sequenced at 2×27 base pairs and with the dual-indexing workflow on an Illumina NovaSeq. Reads were trimmed, merged, and aligned to retrieve probe identity, and the unique molecular identifier of each read was used to remove PCR duplicates converting reads to digital counts for each target within an individual ROI.

Analysis of spatial RNA sequencing data. Counts from each ROI were quantified using the NanoString GeoMx NGS Pipeline. For the ROI analysis, initial quality control was implemented by first identifying low performance probes by dividing the geometric mean of a single probe count across all samples against the geometric mean of all the probe counts for that gene. All probes >0.1 were kept for analysis, as recommended by NanoString (https://bioconductor.org/packages/devel/workflows/vignettes/GeoMxWorkflows/inst/doc/GeomxTools_RNA-NGS_Analysis.html).. To identify samples with high background noise (no-specific probe binding), we first calculated the limit of quantification (LOQ), which is 2 standard deviations above the geometric mean of the negative probes for each sample. The percentage of genes detected above the LOQ value was then calculated and samples removed from the analysis if they fell below a 1% gene detection rate. Additionally, we examined the ratio of the Q3 quartile value against the mean of the geometric mean of the negative probe counts and removed samples with a ratio less than 1, suggesting the signal from the probes in that sample are unreliable. This left 94 ROIs for downstream analysis. Gene counts were normalized using Q3 normalization. Differential expression

within each ROI type (DWM, SWM and DGM) was calculated for each gene using a linear mixed effect model with the Geomx Tools R package (doi: 10.18129/B9.bioc.GeomxTools; **Table S3**), using ZikV exposure as the test variable, with random slope and random intercept for animal ID. This method provides an unadjusted p-value for each gene comparison as well as a false-discovery rate (FDR), which is calculated using the Benjamini-Hochberg method. Gene set enrichment analysis was performed using FGSEA[76] or SetRank[77] with Gene Ontology (GO) biological processes on each set of significant DE genes for each region using log fold changes as the ranking metric (**Table S4**). For gene network analysis, a subset of significantly enriched pathways (FDR<0.05 in at least one comparison; **Table S3**) identified from spatial DE analysis of DWM and DGM were visualized in a gene network using Cytoscape v3.9.1 using Omics Visualizer Viz PieChart plug-in[78] (**Fig. 1f**).

Bulk RNA Sequencing. For each animal, brain was sampled from the rostral-caudal level of five coronal sections and designated as frontal (F), parietal (P1-3), and occipital (O) (**Fig. S1b**). The parietal designations encompassed midline structures, including thalamus and deep nuclei, as well as temporal lobe. Brain samples were immersed immediately in RNALater, stored at 4°C for 24 h, and subsequently homogenized in QIAzol (QIAGEN). RNA was isolated from QIAzol homogenates following the QIAGEN RNeasy protocol. Ribosomal RNA (rRNA) was depleted from each RNA sample using the Ribo-ZerorRNA Removal Kit (Epicentre), designed for human, mouse and rat samples, but is also effective in reducing rRNA amounts for NHP total RNA samples. Libraries were prepared from 150 ng of rRNA-depleted RNA following the KAPA Stranded RNA-Seq with RiboErase workflow for Total RNA-Seq libraries (KAPA Biosystems). Library quality was evaluated using the Qubit® 3.0 Fluorometer and the Agilent 2100 Bioanalyzer instrument. Constructed libraries were sequenced on a NextSeq 500 Illumina platform, producing 2x75nt stranded paired-end reads. Quality control of the primary sequencing data was performed using FastQC. Ribosomal RNA reads were removed computationally using Bowtie2[79], with an index composed of human, mouse and rat rRNA sequences, resulting in over 30 million reads. Sequence reads were trimmed to 50 bp and

362 then aligned to the pig-tailed macaque (*Macaca nemestrina*) genome (Mnem_1.0) using STAR[80].
363 Alignment results show >90% mapping of NHP reads to the pig-tailed genome.

364

365 **Analysis of bulk RNA sequencing data.** Statistical processing and analysis of RNA-seq count data
366 was done with the R statistical computing environment (R Core Team 2019). Gene counts were
367 filtered by a row mean of 3 or greater and then normalized using edgeR to implement TMM
368 normalization[81,82]. Counts were transformed into log-counts for use in a linear model using voom[83].
369 Principle Component Analysis was performed using factoextra. Differential expression (DE) analysis
370 compared each ZIKV (BRZ or FSS) brain sample against its designation-matched CTL sample
371 based on a linear model fit for each gene using Limma[84]. Criteria for all DE analyses were an
372 absolute fold change of 1.5 and an adjusted *P*-value<0.05 calculated using a Benjamini-Hochberg
373 correction. The average log2 fold changes (LFC) of significantly DE genes for each brain region
374 were averaged between BRZ and FSS to illustrate general expression trends across the two ZIKV
375 infections (**Fig. S4c**). Hierarchical clustering was performed on average LFC for DE genes identified
376 in at least one contrast and over representation analysis was performed on each of the clusters using
377 SetRank[77] using KEGG, WikiPathways, and Gene Ontology databases. All gene names were
378 converted to human orthologs and a pathway was considered significantly enriched with an FDR
379 <0.05 (**Table S7**). CIBERSORTx was used to predict cell type abundances in each brain sample by
380 inputting TMM log2 normalized expression values using the single cell reference data set from
381 Darmanis *et al*. 2015 (**Fig. S4d, Table S9**)[33,85].

382

383 **Data and code availability.** Transcriptomics data sets are available in the NCBI Gene Expression
384 Omnibus (GEO) under accession number GSE226401 (bulk RNA-seq) andGSE22753 (spatial
385 transcriptomics). The R codes applied to these analyses can be accessed at

386 https://github.com/galelab/Tisoncik-Go_ZIKA_NHP_FetalBrain and
387 https://github.com/galelab/Tisoncik-Go_ZIKA_NHP_Geomx_FetalBrain BulkRNAseq.
388
389 **Automated Immunohistochemistry staining.** Immunohistochemistry staining was performed for
390 GFAP, Iba1, MBP, NeuN, and Olig2 (**Table S10**) utilizing the Leica Bond Rx Automated
391 Immunostainer (Leica Microsystems, Buffalo Grove, IL). Unless otherwise specified all reagents
392 were obtained from Leica Microsystems. Slides were first deparaffinized with Leica Dewax Solution
393 at 72°C for 30 sec. Antigen retrieval was performed on all slides stained for Iba1 and NeuN with
394 citrate, pH 6, at 100°C for 10 min and Olig2 stained slides for 20 min. Antigen retrieval was performed
395 on all slides stained for MBP with EDTA, pH 9, at 100°C for 20 min. Additionally, antigen retrieval for
396 GFAP consisted of proteinase K digestion at 37°C for 5 min. All subsequent steps were performed
397 at room temperature. Initial blocking consisted of 10% normal goat serum (Jackson
398 ImmunoResearch, Catalog Number 005-000-121) in tris-buffered saline for 20 min. Additional
399 blocking occurred with Leica Bond Peroxide Block for 5 min. Slides were incubated with GFAP
400 (1:500), Iba1 (1:500), or Olig2 (1:500) primary antibodies in Leica Primary Antibody Diluent for 30
401 min. Next, a secondary antibody, goat anti-rabbit horseradish peroxidase polymerized antibody, was
402 applied for 8 min. Slides incubated with MBP (1:500) primary antibody in Leica Primary Antibody
403 Diluent for 30 min was followed by application of a rabbit anti-rat secondary (Vector Laboratories,
404 Catalog Number AI-4001) for 8 min. Slides incubated with NeuN (1:500) primary antibody in Leica
405 Primary Antibody Diluent for 30 min was followed by application of the Leica Post-Primary linker for
406 8 minutes. NeuN-stained tissues were then incubated with a tertiary antibody, goat anti-rabbit
407 horseradish peroxidase polymerized antibody, for 8 min. All antibody complexes were visualized
408 using DAB (3,3'-diaminobenzidine), detection 2X for 10 min. Tissues were counterstained with
409 hematoxylin for 4 min followed by two rinses in deionized water. Slides were removed from the

automated stainer and dehydrated through graded alcohol to xylene. Once dehydrated, slides were coverslipped with a synthetic mounting media and imaged.

Quantitative microscopy and image analyses. Slides were scanned in brightfield with a 20X objective using the NanoZoomer Digital Pathology System (Hamamatsu City, Japan). The digital images were then imported into Visiopharm software (Hoersholm, Denmark) for analysis. Using the Visiopharm Image Analysis module, regions of interests (ROI) were automatically detected around the entire tissue section. The digital images of the Iba1 and MBP slides were converted into grayscale values using two feature bands, RGB – G with a mean 3 x 3 pixel filter and HDAB – DAB. The Visiopharm software was trained to detect positive, Iba1 or MBP, staining and hematoxylin counterstain, based on a threshold of feature band pixel values, creating a project specific configuration. Images were processed in batch mode using this configuration to generate the desired per area outputs. For NeuN quantitation, ROIs were manually drawn in three independent GM regions of the parietal and occipital cortex tissues and subdivided into five tissue layers from each region (**Fig. S6b**). The digital images of the NeuN slides were converted into grayscale values using two feature bands, Chromaticity Red and FastRed_DAB – Fast Red with a mean 7 x 7 pixel filter. The Visiopharm software was trained to detect positive, NeuN, staining and hematoxylin counterstain, based on a threshold of feature band pixel values, creating a project specific configuration. Images were processed in batch mode using this configuration to generate the desired per area outputs. For Olig2 quantitation, ROIs were manually drawn around the white matter. The digital images of the Olig2 slides were converted into grayscale values using two feature bands, HDAB – DAB with a polynomial blob filter and H&E – hematoxylin with a mean 3 x 3 pixel filter and polynomial blob filter. The Visiopharm software was trained to detect Olig2 positive nuclei and negative nuclei based on a threshold of feature band pixel values, creating a project specific

configuration. Images were processed in batch mode using this configuration to generate the desired outputs.

Luxol fast blue-PAS-hematoxylin staining. Luxol fast blue (LFB) combined with the periodic acid-Schiff (PAS) procedure was used for histologic examination of white matter. On tissue slides, LFB stain highlights the blue myelinated axons of neurons in the white matter tracks and the small dense round nuclei of oligodendrocytes that produce myelin. Demyelination is identified as regions of CNS which lose the blue color that the LFB normally confers to myelin. Fixed tissues 10-15 μm thick were sectioned from paraffin blocks and mounted onto slides. Slides were first deparaffinized and tissue sections hydrated with 95% alcohol. Tissue sections were placed in a tightly capped container with LFB solution at 56°C overnight. Sections were rinsed in 95% alcohol to remove excess stain followed by rinses in distilled water. Slides were then immersed in lithium carbonate, 0.05% solution for 10-20 sec followed by immersion in 70% alcohol solution until gray and white matter can be distinguished. The sections were then washed in distilled water. The differentiation was finished by rinsing briefly in lithium carbonate solution and then putting through several changes of 70% alcohol solution until white matter sharply contrasted with the gray matter. The sections were thoroughly rinsed in distilled water and placed in 1% periodic acid solution for 5 min followed by rinsing in 2 changes of distilled water. Sections were then placed in Schiff solution for 15 min and washed in tap water for 5 min. Sections were then dehydrated in 95% alcohol and 2 changes of absolute alcohol. The final step was clearing in 3 changes of xylene and mounting with a synthetic resin.

Magnetic resonance imaging. MRI was performed using a Philips Achieva 3T scanner using acquisition parameters that have been previously described[29]. In brief, a 2D single-shot, half-Fourier turbo spin echo multislice sequence (HASTE) was used to acquire T2-weighted images at various gestational time points (**Fig. S1**). Primary analysis of T2 signal abnormality was performed at a single time point representing late gestation for which all animals had imaging (approximately GD120). To

quantify the magnitude of the T2 signal abnormality in white matter, a scale from 0-3 was devised, corresponding to normal, mild, moderate, and severe abnormality. A score of 0 reflected the expected signal intensity based on control animals and a score of 3 reflected increased signal intensity matching the signal from surrounding CSF, which was typically the intensity of the primary periventricular lesion in affected animals. Image quality and stability was insufficient to perform analysis of diffusion tensor imaging.

Electron microscopy analysis. Tissue was fixed in 4% glutaraldehyde in sodium cacodylate buffer at a pH of 7.3, at room temperature, then stored overnight at 4°C. The tissue was then washed 5 times in buffer, then post fixed in 2% buffered osmium tetroxide for 1 hour, on ice. The tissue was then washed 5 times in water, dehydrated in a graded series of alcohol, then propylene oxide twice. This was followed by infiltration in 1:1 propylene oxide: epon araldite, 2 changes of epon araldite, and finally polymerization overnight in an oven at 60°C. Sections of 80 nm thickness were collected on formvar coated slot grids and imaged at 80KV on a JEOL1230 TEM. A formar grid was used to define consistent regions of analysis in all sections assessed. All axons within five fields of view were analyzed. Ten high-power images (10,000 x magnification) within a field of view were generated. ImageJ analysis software was used to measure the axon diameter, fiber diameter (both the axon and myelin sheath) and myelin sheath thickness. The g-ratio was only measured in areas of compact myelin and calculated as the outer diameter across the axon divided by the outer diameter across the axon and myelin sheath measured at the same point.

Author Contributions

JT-G and CS wrote the manuscript, with input from other authors, and coordinated contributions between the collaborating laboratories. MG Jr., KAW and LR oversaw the NHP model at the Washington National Primate Research Center. RPK performed the fetal brain necropsy and collected samples. KV participated in sample collection and processing for RNA analysis. JSB performed the viral qRT-PCR assay. JMS performed the histopathologic assessment of brain tissues. EP prepared the specimens for electron microscopy and operated the transmission electron microscope. JT-G collected electron microscopy images and CS performed electron microscopy analysis. JT-G and CS performed immunohistochemical analyses. CS and DS performed MRI analysis. JT-G processed samples for transcriptome sequencing. ES constructed bulk RNAseq libraries and performed the library sequencing. ATG performed the GeoMx DSP assay on control specimens. LSW and DN performed the spatial and bulk transcriptomic analyses. JT-G and CS provided the associated functional interpretation of the transcriptomic datasets. All authors reviewed the final draft of the manuscript. The authors declare no competing financial interests.

Acknowledgements

We acknowledge Audrey Baldessari, Chris English, Jason Ogle, Audrey Germond, and W. McIntyre Durning at the Washington National Primate Research Center for their contributions to the study execution. We thank Jonah Chan (UCSF) for providing input on experiments, Steve Perlmutter (UW) and Philip Horner (Houston Methodist Research Institute) for valuable discussions of the electron microscopy data. We acknowledge Bethany Kondiles (UW) for guidance on electron microscopy analysis and Erica Boldenow (SCRI) for technical support. Funding for this study was supported by 5R01AI143265 (MG and KAW) and AI145296 (MG), K08AI150996 (CS), and Core Grant for Vision Research NEI P30EY001730. We thank the University of Washington Histology and Imaging Core, Seattle Genomics Core lab, and NanoString Technologies (Seattle, WA) for their services. Funding for Seattle Genomics is supported in part by the National Institutes of Health, Office of the Director P51OD010425 (Seattle MG). Instrumentation used for the GeoMx DSP experiment was supported with Federal funds from the National Institute of Allergy and Infectious Diseases, National Institutes of Health, Department of Health and Human Services, under Contract No. HHSN272201800008C.

References

1 Leal, M. C. *et al.* Hearing Loss in Infants with Microcephaly and Evidence of Congenital Zika Virus Infection - Brazil, November 2015-May 2016. *MMWR Morb Mortal Wkly Rep* **65**, 917-919, doi:10.15585/mmwr.mm6534e3 (2016).

2 de Paula Freitas, B. *et al.* Ocular Findings in Infants With Microcephaly Associated With Presumed Zika Virus Congenital Infection in Salvador, Brazil. *JAMA Ophthalmol*, doi:10.1001/jamaophthalmol.2016.0267 (2016).

3 Brasil, P. *et al.* Zika Virus Infection in Pregnant Women in Rio de Janeiro. *N Engl J Med* **375**, 2321-2334, doi:10.1056/NEJMoa1602412 (2016).

4 Mlakar, J. *et al.* Zika Virus Associated with Microcephaly. *The New England journal of medicine* **374**, 951-958, doi:10.1056/NEJMoa1600651 (2016).

5 Driggers, R. W. *et al.* Zika Virus Infection with Prolonged Maternal Viremia and Fetal Brain Abnormalities. *N Engl J Med* **374**, 2142-2151, doi:10.1056/NEJMoa1601824 (2016).

6 Meaney-Delman, D. *et al.* Zika Virus Infection Among U.S. Pregnant Travelers - August 2015-February 2016. *MMWR Morb Mortal Wkly Rep* **65**, 211-214, doi:10.15585/mmwr.mm6508e1 (2016).

7 van der Eijk, A. A. *et al.* Miscarriage Associated with Zika Virus Infection. *N Engl J Med* **375**, 1002-1004, doi:10.1056/NEJMc1605898 (2016).

8 Matiello, F. B., Hilario, J. S. M., Gondim, E. C., Santos, D. N. & Mello, D. F. Health surveillance and development of children with congenital Zika Virus syndrome: an integrative literature review. *Rev Paul Pediatr* **40**, e2020335, doi:10.1590/1984-0462/2022/40/2020335 (2021).

9 Sanders Pereira Pinto, P. *et al.* Brain abnormalities on neuroimaging in Children with Congenital Zika Syndrome in Salvador, Brazil, and its possible implications on neuropsychological development. *Int J Dev Neurosci* **80**, 189-196, doi:10.1002/jdn.10016 (2020).

10 Dang, J. *et al.* Zika Virus Depletes Neural Progenitors in Human Cerebral Organoids through Activation of the Innate Immune Receptor TLR3. *Cell Stem Cell* **19**, 258-265, doi:10.1016/j.stem.2016.04.014 (2016).

11 Tang, H. *et al.* Zika Virus Infects Human Cortical Neural Progenitors and Attenuates Their Growth. *Cell Stem Cell* **18**, 587-590, doi:10.1016/j.stem.2016.02.016 (2016).

12 Li, C. *et al.* Zika Virus Disrupts Neural Progenitor Development and Leads to Microcephaly in Mice. *Cell Stem Cell* **19**, 120-126, doi:10.1016/j.stem.2016.04.017 (2016).

13 Chang, K. J., Redmond, S. A. & Chan, J. R. Remodeling myelination: implications for mechanisms of neural plasticity. *Nat Neurosci* **19**, 190-197, doi:10.1038/nn.4200 (2016).

14 Monje, M. Myelin Plasticity and Nervous System Function. *Annu Rev Neurosci* **41**, 61-76, doi:10.1146/annurev-neuro-080317-061853 (2018).

15 Buyanova, I. S. & Arsalidou, M. Cerebral White Matter Myelination and Relations to Age, Gender, and Cognition: A Selective Review. *Front Hum Neurosci* **15**, 662031, doi:10.3389/fnhum.2021.662031 (2021).

16 Deoni, S. C. *et al.* Mapping infant brain myelination with magnetic resonance imaging. *J Neurosci* **31**, 784-791, doi:10.1523/JNEUROSCI.2106-10.2011 (2011).

17 Hasegawa, M. *et al.* Development of myelination in the human fetal and infant cerebrum: a myelin basic protein immunohistochemical study. *Brain Dev* **14**, 1-6, doi:10.1016/s0387-7604(12)80271-3 (1992).

18 McKenzie, I. A. *et al.* Motor skill learning requires active central myelination. *Science* **346**, 318-322, doi:10.1126/science.1254960 (2014).

19 Makinodan, M., Rosen, K. M., Ito, S. & Corfas, G. A critical period for social experience-dependent oligodendrocyte maturation and myelination. *Science* **337**, 1357-1360, doi:10.1126/science.1220845 (2012).

20 Scholz, J., Klein, M. C., Behrens, T. E. & Johansen-Berg, H. Training induces changes in white-matter architecture. *Nat Neurosci* **12**, 1370-1371, doi:10.1038/nn.2412 (2009).

21 Pan, S., Mayoral, S. R., Choi, H. S., Chan, J. R. & Kheirbek, M. A. Preservation of a remote fear memory requires new myelin formation. *Nat Neurosci* **23**, 487-499, doi:10.1038/s41593-019-0582-1 (2020).

22 Wang, F. *et al.* Enhancing Oligodendrocyte Myelination Rescues Synaptic Loss and Improves Functional Recovery after Chronic Hypoxia. *Neuron* **99**, 689-701 e685, doi:10.1016/j.neuron.2018.07.017 (2018).

23 Kadhim, H. *et al.* Inflammatory cytokines in the pathogenesis of periventricular leukomalacia. *Neurology* **56**, 1278-1284, doi:10.1212/wnl.56.10.1278 (2001).

24 Nguyen, S. M. *et al.* Highly efficient maternal-fetal Zika virus transmission in pregnant rhesus macaques. *PLoS Pathog* **13**, e1006378, doi:10.1371/journal.ppat.1006378 (2017).

25 Coffey, L. L. *et al.* Intraamniotic Zika virus inoculation of pregnant rhesus macaques produces fetal neurologic disease. *Nat Commun* **9**, 2414, doi:10.1038/s41467-018-04777-6 (2018).

26 Martinot, A. J. *et al.* Fetal Neuropathology in Zika Virus-Infected Pregnant Female Rhesus Monkeys. *Cell* **173**, 1111-1122 e1110, doi:10.1016/j.cell.2018.03.019 (2018).

27 Dudley, D. M. *et al.* Miscarriage and stillbirth following maternal Zika virus infection in nonhuman primates. *Nat Med* **24**, 1104-1107, doi:10.1038/s41591-018-0088-5 (2018).

28 Adams Waldorf, K. M. *et al.* Fetal brain lesions after subcutaneous inoculation of Zika virus in a pregnant nonhuman primate. *Nature medicine* **22**, 1256-1259, doi:10.1038/nm.4193 (2016).

29 Adams Waldorf, K. M. *et al.* Congenital Zika virus infection as a silent pathology with loss of neurogenic output in the fetal brain. *Nat Med* **24**, 368-374, doi:10.1038/nm.4485 (2018).

30 Weng, C., Ding, M., Fan, S., Cao, Q. & Lu, Z. Transcription factor 7 like 2 promotes oligodendrocyte differentiation and remyelination. *Mol Med Rep* **16**, 1864-1870, doi:10.3892/mmr.2017.6843 (2017).

31 Zhao, C. T. *et al.* Dual regulatory switch through interactions of Tcf7l2/Tcf4 with stage-specific partners propels oligodendroglial maturation. *Nature Communications* **7**, doi:ARTN 10883

10.1038/ncomms10883 (2016).

32 Emery, B. & Lu, Q. R. Transcriptional and Epigenetic Regulation of Oligodendrocyte Development and Myelination in the Central Nervous System. *Cold Spring Harb Perspect Biol* **7**, a020461, doi:10.1101/cshperspect.a020461 (2015).

33 Newman, A. M. *et al.* Determining cell type abundance and expression from bulk tissues with digital cytometry. *Nat Biotechnol* **37**, 773-782, doi:10.1038/s41587-019-0114-2 (2019).

34 Arnett, H. A. *et al.* bHLH transcription factor Olig1 is required to repair demyelinated lesions in the CNS. *Science* **306**, 2111-2115, doi:10.1126/science.1103709 (2004).

35 Zhou, Q., Wang, S. & Anderson, D. J. Identification of a novel family of oligodendrocyte lineage-specific basic helix-loop-helix transcription factors. *Neuron* **25**, 331-343, doi:10.1016/s0896-6273(00)80898-3 (2000).

36 Riddle, A. *et al.* Histopathological correlates of magnetic resonance imaging-defined chronic perinatal white matter injury. *Ann Neurol* **70**, 493-507, doi:10.1002/ana.22501 (2011).

37 Payne, S. C., Bartlett, C. A., Harvey, A. R., Dunlop, S. A. & Fitzgerald, M. Myelin sheath decompaction, axon swelling, and functional loss during chronic secondary degeneration in rat optic nerve. *Invest Ophthalmol Vis Sci* **53**, 6093-6101, doi:10.1167/iovs.12-10080 (2012).

38 Popko, B. *et al.* Myelin deficient mice: expression of myelin basic protein and generation of mice with varying levels of myelin. *Cell* **48**, 713-721, doi:10.1016/0092-8674(87)90249-2 (1987).

39 Tognatta, R. *et al.* Astrocytes Are Required for Oligodendrocyte Survival and Maintenance of Myelin Compaction and Integrity. *Front Cell Neurosci* **14**, 74, doi:10.3389/fncel.2020.00074 (2020).

40 Weil, M. T. *et al.* Loss of Myelin Basic Protein Function Triggers Myelin Breakdown in Models of Demyelinating Diseases. *Cell Rep* **16**, 314-322, doi:10.1016/j.celrep.2016.06.008 (2016).

41 Stikov, N. *et al.* Quantitative analysis of the myelin g-ratio from electron microscopy images of the macaque corpus callosum. *Data Brief* **4**, 368-373, doi:10.1016/j.dib.2015.05.019 (2015).

42 Ribeiro, C. T. M. *et al.* Gross motor function in children with Congenital Zika Syndrome from Rio de Janeiro, Brazil. *Eur J Pediatr* **181**, 783-788, doi:10.1007/s00431-021-04270-1 (2022).

43 Valdes, V. *et al.* Cognitive Development of Infants Exposed to the Zika Virus in Puerto Rico. *JAMA Netw Open* **2**, e1914061, doi:10.1001/jamanetworkopen.2019.14061 (2019).

44 Nielsen-Saines, K. *et al.* Delayed childhood neurodevelopment and neurosensory alterations in the second year of life in a prospective cohort of ZIKV-exposed children. *Nat Med* **25**, 1213-1217, doi:10.1038/s41591-019-0496-1 (2019).

45 Vouga, M., Pomar, L., Panchaud, A., Musso, D. & Baud, D. A critical analysis of the neurodevelopmental and neurosensory outcomes after 2 years for children with in utero Zika virus exposure. *Nat Med* **25**, 1641-1642, doi:10.1038/s41591-019-0630-0 (2019).

46 Mulkey, S. B. *et al.* Neurodevelopmental Abnormalities in Children With In Utero Zika Virus Exposure Without Congenital Zika Syndrome. *JAMA Pediatr* **174**, 269-276, doi:10.1001/jamapediatrics.2019.5204 (2020).

47 Cavalcante, T. B. *et al.* Congenital Zika syndrome: Growth, clinical, and motor development outcomes up to 36 months of age and differences according to microcephaly at birth. *Int J Infect Dis* **105**, 399-408, doi:10.1016/j.ijid.2021.02.072 (2021).

48 Mavigner, M. *et al.* Postnatal Zika virus infection is associated with persistent abnormalities in brain structure, function, and behavior in infant macaques. *Sci Transl Med* **10**, doi:10.1126/scitranslmed.aao6975 (2018).

49 Seferovic, M. *et al.* Experimental Zika Virus Infection in the Pregnant Common Marmoset Induces Spontaneous Fetal Loss and Neurodevelopmental Abnormalities. *Sci Rep* **8**, 6851, doi:10.1038/s41598-018-25205-1 (2018).

50 Gurung, S. *et al.* Zika virus infection at mid-gestation results in fetal cerebral cortical injury and fetal death in the olive baboon. *PLoS Pathog* **15**, e1007507, doi:10.1371/journal.ppat.1007507 (2019).

51 Cumberworth, S. L. *et al.* Zika virus tropism and interactions in myelinating neural cell cultures: CNS cells and myelin are preferentially affected. *Acta Neuropathol Commun* **5**, 50, doi:10.1186/s40478-017-0450-8 (2017).

52 Li, Q. *et al.* Ultrastructural Characteristics of Neuronal Death and White Matter Injury in Mouse Brain Tissues After Intracerebral Hemorrhage: Coexistence of Ferroptosis, Autophagy, and Necrosis. *Front Neurol* **9**, 581, doi:10.3389/fneur.2018.00581 (2018).

53 Schultz, V. *et al.* Zika Virus Infection Leads to Demyelination and Axonal Injury in Mature CNS Cultures. *Viruses* **13**, doi:10.3390/v13010091 (2021).

54 Fancy, S. P., Zhao, C. & Franklin, R. J. Increased expression of Nkx2.2 and Olig2 identifies reactive oligodendrocyte progenitor cells responding to demyelination in the adult CNS. *Mol Cell Neurosci* **27**, 247-254, doi:10.1016/j.mcn.2004.06.015 (2004).

55 Tripathi, R. B., Rivers, L. E., Young, K. M., Jamen, F. & Richardson, W. D. NG2 glia generate new oligodendrocytes but few astrocytes in a murine experimental autoimmune encephalomyelitis model of demyelinating disease. *J Neurosci* **30**, 16383-16390, doi:10.1523/JNEUROSCI.3411-10.2010 (2010).

56 Zawadzka, M. *et al.* CNS-resident glial progenitor/stem cells produce Schwann cells as well as oligodendrocytes during repair of CNS demyelination. *Cell Stem Cell* **6**, 578-590, doi:10.1016/j.stem.2010.04.002 (2010).

57 Back, S. A. White matter injury in the preterm infant: pathology and mechanisms. *Acta Neuropathol* **134**, 331-349, doi:10.1007/s00401-017-1718-6 (2017).

58 Haynes, R. L. *et al.* Nitrosative and oxidative injury to premyelinating oligodendrocytes in periventricular leukomalacia. *J Neuropathol Exp Neurol* **62**, 441-450, doi:10.1093/jnen/62.5.441 (2003).

59 Carteaux, G. *et al.* Zika Virus Associated with Meningoencephalitis. *N Engl J Med* **374**, 1595-1596, doi:10.1056/NEJMc1602964 (2016).

60 Neri, V. C. *et al.* Case Report: Acute Transverse Myelitis after Zika Virus Infection. *Am J Trop Med Hyg* **99**, 1419-1421, doi:10.4269/ajtmh.17-0938 (2018).

61 Jurado, K. A. *et al.* Antiviral CD8 T cells induce Zika-virus-associated paralysis in mice. *Nat Microbiol* **3**, 141-147, doi:10.1038/s41564-017-0060-z (2018).

62 Cao-Lormeau, V. M. *et al.* Guillain-Barre Syndrome outbreak associated with Zika virus infection in French Polynesia: a case-control study. *Lancet* **387**, 1531-1539, doi:10.1016/S0140-6736(16)00562-6 (2016).

63 Soares, C. N. *et al.* Fatal encephalitis associated with Zika virus infection in an adult. *J Clin Virol* **83**, 63-65, doi:10.1016/j.jcv.2016.08.297 (2016).

64 Back, S. A. & Miller, S. P. Brain injury in premature neonates: A primary cerebral dysmaturation disorder? *Ann Neurol* **75**, 469-486, doi:10.1002/ana.24132 (2014).

65 Back, S. A. & Rosenberg, P. A. Pathophysiology of glia in perinatal white matter injury. *Glia* **62**, 1790-1815, doi:10.1002/glia.22658 (2014).

66 Giacci, M. K. *et al.* Three dimensional electron microscopy reveals changing axonal and myelin morphology along normal and partially injured optic nerves. *Sci Rep* **8**, 3979, doi:10.1038/s41598-018-22361-2 (2018).

67 Gutierrez, R., Boison, D., Heinemann, U. & Stoffel, W. Decompaction of CNS myelin leads to a reduction of the conduction velocity of action potentials in optic nerve. *Neurosci Lett* **195**, 93-96, doi:10.1016/0304-3940(94)11789-l (1995).

68 Knowles, J. K., Batra, A., Xu, H. & Monje, M. Adaptive and maladaptive myelination in health and disease. *Nat Rev Neurol* **18**, 735-746, doi:10.1038/s41582-022-00737-3 (2022).

69 Garber, C. *et al.* T cells promote microglia-mediated synaptic elimination and cognitive dysfunction during recovery from neuropathogenic flaviviruses. *Nat Neurosci* **22**, 1276-1288, doi:10.1038/s41593-019-0427-y (2019).

70 Choi, J. T., Vining, E. P., Mori, S. & Bastian, A. J. Sensorimotor function and sensorimotor tracts after hemispherectomy. *Neuropsychologia* **48**, 1192-1199, doi:10.1016/j.neuropsychologia.2009.12.013 (2010).

71 Fiori, S. & Guzzetta, A. Plasticity following early-life brain injury: Insights from quantitative MRI. *Semin Perinatol* **39**, 141-146, doi:10.1053/j.semperi.2015.01.007 (2015).

72 Malhotra, B. *et al.* Clinico-epidemiological and genomic profile of first Zika Virus outbreak in India at Jaipur city of Rajasthan state. *J Infect Public Health* **13**, 1920-1926, doi:10.1016/j.jiph.2020.10.006 (2020).

73 Coutinho, R. Z., Montalvo, A. V., Weitzman, A. & Marteleto, L. J. Zika virus public health crisis and the perpetuation of gender inequality in Brazil. *Reprod Health* **18**, 40, doi:10.1186/s12978-021-01067-1 (2021).

74 Goyal, D. & Selix, N. W. Impact of COVID-19 on Maternal Mental Health. *MCN Am J Matern Child Nurs* **46**, 103-109, doi:10.1097/NMC.0000000000000692 (2021).

75 Vouga, M. *et al.* Maternal outcomes and risk factors for COVID-19 severity among pregnant women. *Sci Rep* **11**, 13898, doi:10.1038/s41598-021-92357-y (2021).

76 Korotkevich, G. *et al.* Fast gene set enrichment analysis. *bioRxiv*, 060012, doi:10.1101/060012 (2021).

77 Simillion, C., Liechti, R., Lischer, H. E., Ioannidis, V. & Bruggmann, R. Avoiding the pitfalls of gene set enrichment analysis with SetRank. *BMC Bioinformatics* **18**, 151, doi:10.1186/s12859-017-1571-6 (2017).

78 Shannon, P. *et al.* Cytoscape: a software environment for integrated models of biomolecular interaction networks. *Genome Res* **13**, 2498-2504, doi:10.1101/gr.1239303 (2003).

79 Langmead, B. & Salzberg, S. L. Fast gapped-read alignment with Bowtie 2. *Nat Methods* **9**, 357-359, doi:10.1038/nmeth.1923 (2012).

80 Dobin, A. *et al.* STAR: ultrafast universal RNA-seq aligner. *Bioinformatics* **29**, 15-21, doi:10.1093/bioinformatics/bts635 (2013).

81 Robinson, M. D., McCarthy, D. J. & Smyth, G. K. edgeR: a Bioconductor package for differential expression analysis of digital gene expression data. *Bioinformatics* **26**, 139-140, doi:10.1093/bioinformatics/btp616 (2010).

82 McCarthy, D. J., Chen, Y. & Smyth, G. K. Differential expression analysis of multifactor RNA-Seq experiments with respect to biological variation. *Nucleic Acids Res* **40**, 4288-4297, doi:10.1093/nar/gks042 (2012).

83 Law, C. W., Chen, Y., Shi, W. & Smyth, G. K. voom: Precision weights unlock linear model analysis tools for RNA-seq read counts. *Genome Biol* **15**, R29, doi:10.1186/gb-2014-15-2-r29 (2014).

84 Ritchie, M. E. *et al.* limma powers differential expression analyses for RNA-sequencing and microarray studies. *Nucleic Acids Res* **43**, e47, doi:10.1093/nar/gkv007 (2015).

85 Darmanis, S. *et al.* A survey of human brain transcriptome diversity at the single cell level. *Proc Natl Acad Sci U S A* **112**, 7285-7290, doi:10.1073/pnas.1507125112 (2015).

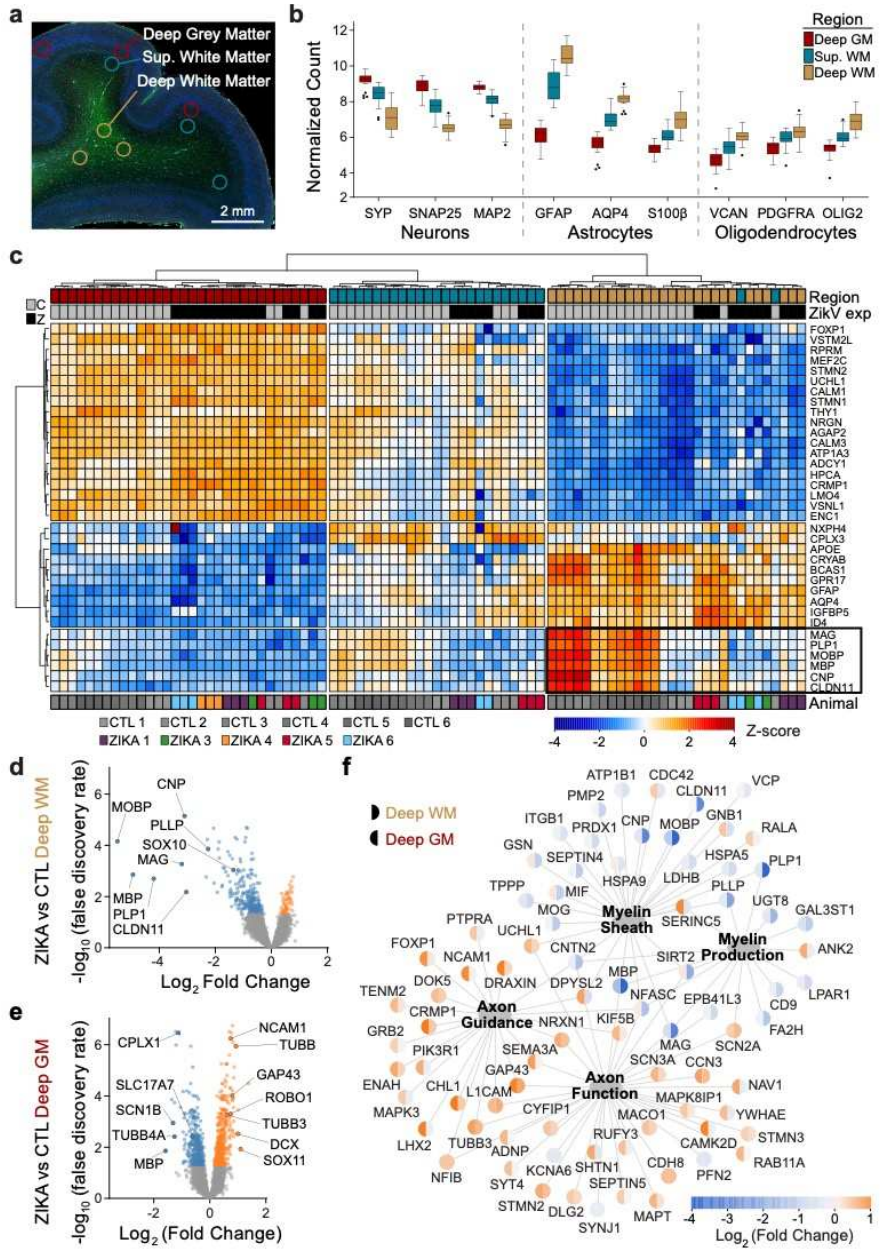

Fig. 1. Congenital Zika infection causes downregulation of myelination genes in deep white matter of nonhuman primate. Digital spatial profiling (DSP) of tissue was conducted using the Nanostring GeoMx DSP platform, after immunofluorescence staining to identify regions of brain and cell types. **a**) ROIs were selected in triplicate for each brain, representing DGM (red), SWM (teal) and DWM (tan). **b**) Tukey plot representing normalized counts for selected genes classically expressed by neurons (left), astrocytes (center), and oligodendrocytes (right), according to ROI. **c**) Normalized gene expression (row-specific Z-score) of the top 35 differentially expressed (DE) genes identified in pair-wise comparison of samples across ROI and ZikV exposure. Samples (x-axis) and genes (y-axis) were clustered by calculating Euclidean distances using Ward.D2. Top row, color coding by ROI, as in panel b. Second row, color coding by exposure: grey, control; black, ZikV. Bottom row: color coding by animal. Black outline identifies genes in DWM, all of which relate to myelination. **d-e**) Volcano plots of DE genes comparing ZikV to control animals for ROIs representing **d**) DWM and **e**) DGM. Orange, significantly (FDR<0.05) upregulated in ZikV; blue, significantly downregulated in ZikV; grey, FDR>0.05 in DE comparison. **f**) Network of 79 DE genes (FDR<0.05) in either DWM or DGM clustered by gene ontology (GO, large nodes) representing axon function (GO:0030424 and GO:0007411) and myelination (GO:0042552 and GO:0043209). GO terms were selected by applying over-representation analysis (ORA) to DE genes in each cluster (**Fig. S2a**). Small nodes represent average log-fold change (color) for each gene in DWM (left half) and DGM (right half). Average gestational age (±SD) of ZikV-exposed vs CTL animals in DSP analysis=150(±9) vs 156(±2) days; p=0.14 by t-test for DGM; 154(±8) vs 156(±2) days; p=0.46 by t-test for DWM.

Figure 2

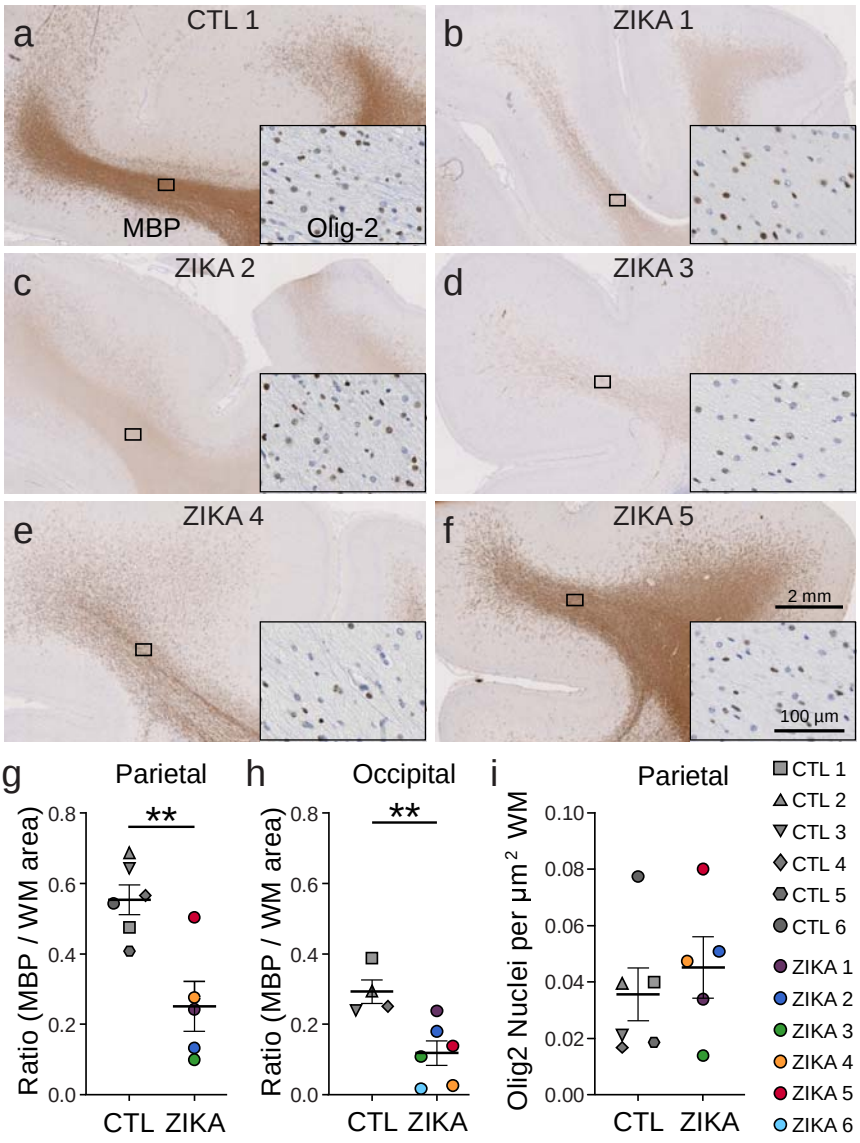

Fig. 2. Immunohistochemical analysis demonstrates marked reduction in myelin basic protein (MBP) in ZikV-exposed fetal NHP brains. a-f, MBP (primary image) and Olig2 (inset) immunohistochemical staining of a) control and b-f) ZikV animals. The representative images are taken from dorsal parietal cortex; the black rectangle identifies the approximate location in the DWM tracts represented in the inset. g-h) Quantification of MBP staining in the DWM from g) parietal and h) occipital cortex, measured as the ratio of area occupied by chromogen divided by the total area of the DWM. i) Quantification of the density of Olig2+ nuclei within the DWM. Points in the plots represent individual animals (one slice per animal was quantified), with bars indicating mean ± SEM. **p<0.01 by unpaired t-test with Welch's correction. Average gestational age (± SD) of ZikV-exposed vs CTL animals in IHC analysis=152(±2) vs 157(±9) days; p=0.23 by t-test.

Figure 3

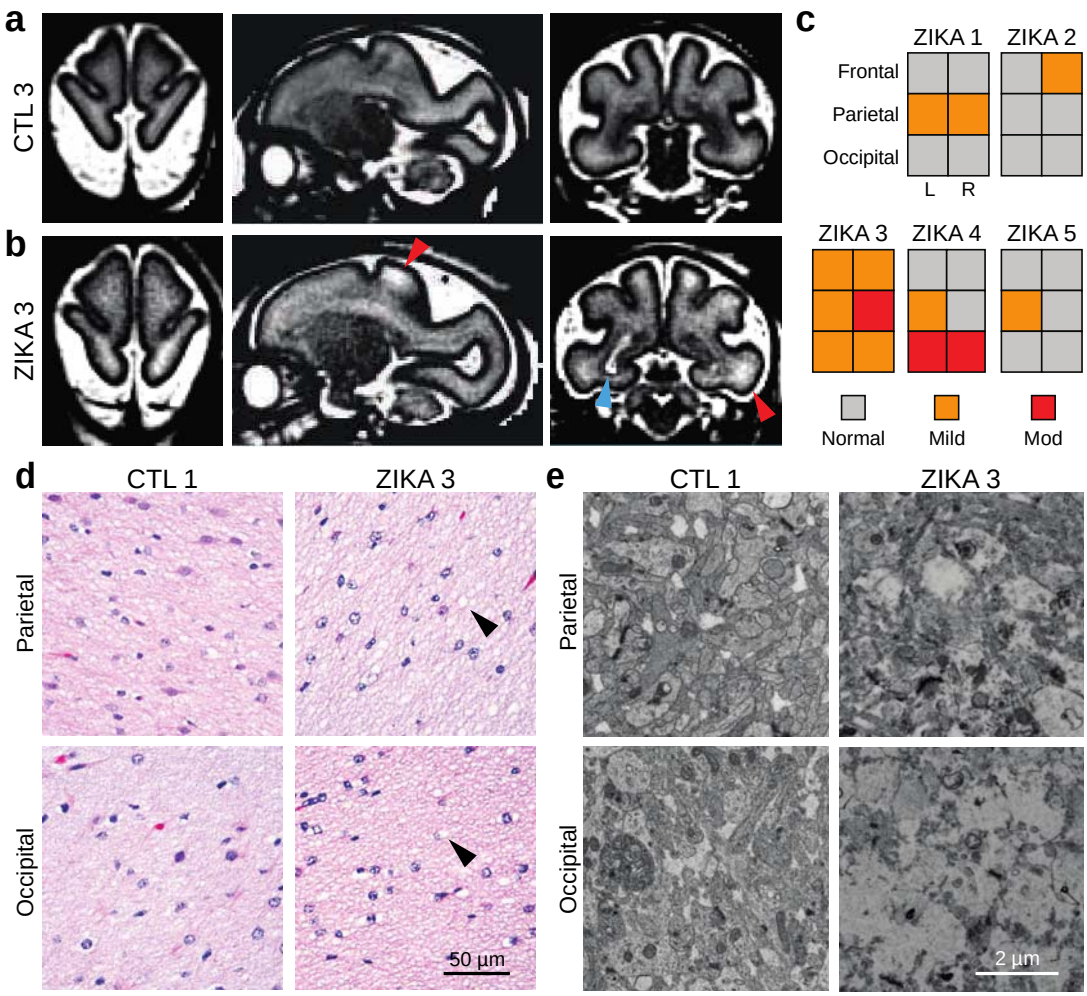

Fig. 3. Spatial heterogeneity of pathology in ZikV-exposed fetal NHP brain. a-b, Representative T2-weighted MRI images (left, axial; middle, sagittal; right, coronal) for a) control and b) ZikV animals. MRI scans were collected at GD125 for CTL3 and GD120 for ZIKA3 (Fig. S1). Blue arrowhead indicates the "primary" periventricular lesion described previously[29]. Red arrowheads indicate T2-weighted (T2W) hyperintense foci in subcortical white matter, which can be seen in delayed, abnormal, or inflamed myelin. c) Ordinal scale of T2W intensity identified in the frontal, parietal and occipital lobes of Zika-exposed animals. Relative scale was established with normal appearance matching control animals and severe signal abnormality matching the T2W signal of the primary lesion. d) Representative hematoxylin and eosin (H&E) images of white matter at the level of parietal lobe (top) and occipital lobe (bottom) for control (left) and ZikV animals (right). Arrowheads indicate areas of vacuolization seen in the H&E staining of white matter of ZikV animals. e) Representative EM images of brain tissue collected from approximate focal areas with T2 signal at the level of parietal lobe (top) and occipital lobe (bottom) for CTL (left) and ZikV animals (bottom). MRI, magnetic resonance imaging.

Figure 4

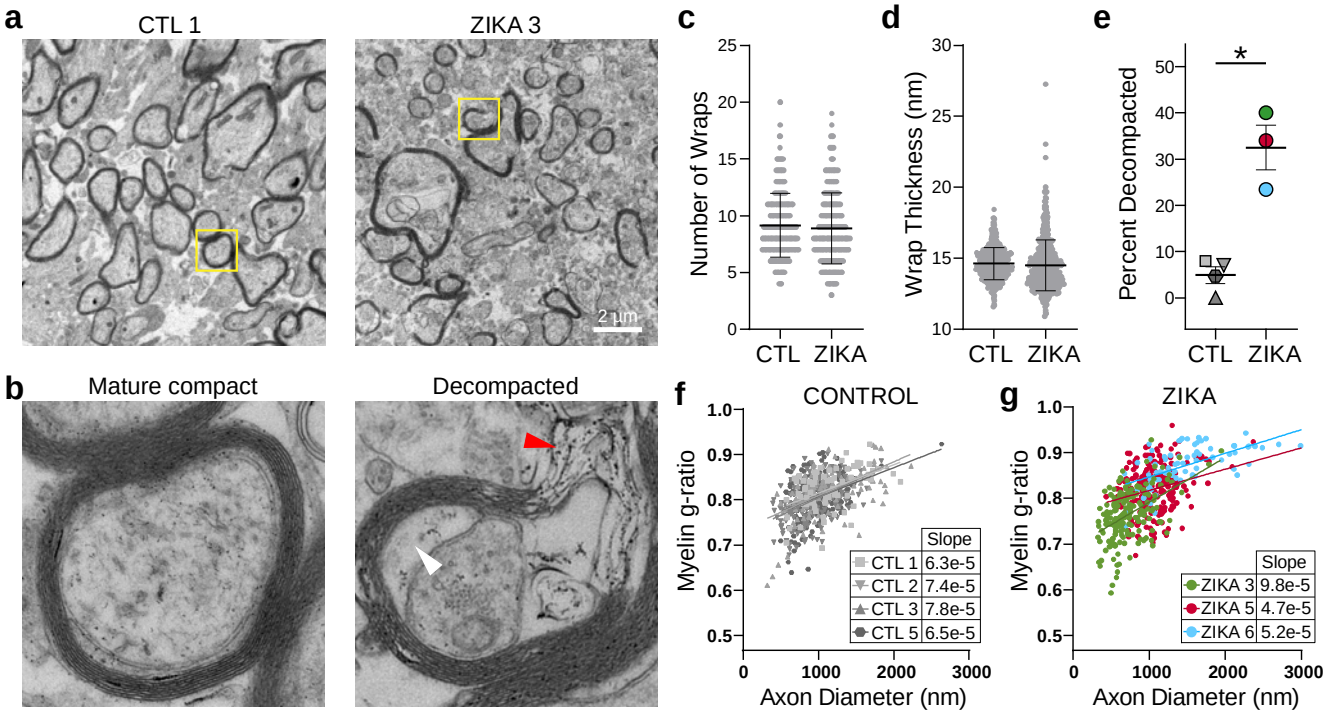

Fig. 4. ZikV exposure is associated with myelin sheath decompaction in fetal NHP brain. EM analysis of brain sections sampled from DWM in parietal cortex. a-b) Representative EM images of myelinated axons from a control (left) and ZikV-exposed animal (right). The area marked by the yellow rectangle is expanded in panel b), demonstrating mature compact myelin (left) and decompacted myelin (right) with electron-dense material in the interlamellar space (red arrowhead) and swelling of the inter lamella (white arrowhead). c-d) Quantification of specific myelin features including the number of c) myelin wraps and d) average wrap thickness for CTL and ZikV animals, measured in areas of compact myelin. Individual points represent data for a single axon; error bars represent mean ± SEM across all points within a treatment condition. e) Percent of axons demonstrating a decompaction phenotype as defined by delamination of all layers of the myelin sheath with outward bowing, affecting at least 25% of the circumference of the axon. Individual points represent, for a single animal, the percent of myelinated axons with decompaction; error bars represent mean ± SEM across all points within a condition. *p<0.05. f-g) Plot of myelin g-ratio (outer diameter of axon divided by outer diameter of myelin sheath, measured in areas of compact myelin) versus axon diameter. Individual points represent a single myelinated axon. Linear regression was calculated for all points representing a single animal; slope is indicated in the table.